

Stochastic Core Spin-Up in Massive Stars – Implications of 3D Simulations of Oxygen Shell Burning

Lucy O. McNeill^{1*} and Bernhard Müller¹

¹ *School of Physics and Astronomy, Monash University, Victoria 3800, Australia*

Accepted XXX. Received YYY; in original form ZZZ

ABSTRACT

It has been suggested based on analytic theory that even in non-rotating supernova progenitors stochastic spin-up by internal gravity waves (IGWs) during the late burning stages can impart enough angular momentum to the core to result in neutron star birth spin periods below 100 ms, and a relatively firm upper limit of 500 ms for the spin period. We here investigate this process using a 3D simulation of oxygen shell burning in a $3M_{\odot}$ He star. Our model indicates that stochastic spin-up by IGWs is less efficient than previously thought. We find that the stochastic angular momentum flux carried by waves excited at the shell boundary is significantly smaller for a given convective luminosity and turnover time than would be expected from simple dimensional analysis. This can be explained by noting that the waves launched by overshooting convective plumes contain modes of opposite angular wave number with similar amplitudes, so that the net angular momentum of excited wave packets almost cancels. We find that the wave-mediated angular momentum flux from the oxygen shell follows a random walk, but again dimensional analysis overestimates the random walk amplitudes since the correlation time is only a fraction of the convective turnover time. Extrapolating our findings over the entire life time of the last burning stages prior to collapse, we predict that the core angular momentum from stochastic spin-up would translate into long birth spin periods of several seconds for low-mass progenitors and no less than 100 ms even for high-mass progenitors.

Key words: waves — hydrodynamics — stars: evolution — stars: massive — stars: interiors — stars: neutron

1 INTRODUCTION

The birth spin periods of pulsars potentially provide a window into the inner workings of angular momentum transport in massive stars and of the core-collapse supernova explosion mechanism. The bulk of the observed solitary neutron star population has birth spin periods of hundreds of ms, and some as fast as tens of ms (Faucher-Giguère & Kaspi 2006; Popov et al. 2010; Popov & Turolla 2012; Gullón et al. 2014). Slow birth spin periods of several hundred ms can be inferred from age and spin down measurements (e.g., PSR J1955+5059 in Noutsos et al. 2013), but without independent measures of the age and braking index, the slow end of the population cannot be tightly constrained. Even for young pulsars with spin periods of >100 ms (e.g. PSR J0248+6021, which has a spin period of 217 ms and age 62 kyr Theureau et al. 2011), uncertainties in possible instabilities and spin-down mechanisms during the first years means that one needs to be careful in drawing con-

clusions from such low spin rates on the birth spin period. Despite long-standing efforts to understand the pre-collapse spin periods of massive stars (e.g., Heger et al. 2000; Hirschi et al. 2004; Heger et al. 2005) and spin-up/spin-down processes during the supernova explosion (Blondin & Mezzacappa 2007; Rantsiou et al. 2011; Wongwathanarat et al. 2013; Kazeroni et al. 2016; Müller et al. 2019; Stockinger et al. 2020), it is still not clear what shapes the observed period distribution.

In particular, there are still considerable uncertainties concerning the angular momentum transport processes in stellar interiors that determine the pre-collapse rotation profiles of massive stars. Stellar evolution models incorporating magnetic torques (e.g., Heger et al. 2005; Suijs et al. 2008; Cantiello et al. 2014) from the Tayler-Spruit dynamo (Spruit 2002) have long defined the state of the art for the treatment of stellar rotation in massive stars. In recent years, however, asteroseismology has revealed unexpectedly slow core rotation rates in low-mass red giants (Beck et al. 2012, 2014; Deheuvels et al. 2012, 2014; Mosser et al. 2012), which cannot be explained by the classic Tayler-Spruit dynamo, suggesting

* E-mail: lucy.mcneill@monash.edu

that even more efficient angular momentum transport mechanisms must operate in nature (Fuller et al. 2014; Cantiello et al. 2014; Wheeler et al. 2015).

Different solutions have been proposed to resolve this problem. Fuller et al. (2019) have proposed a modification of the Tayler-Spruit dynamo which efficiently slows down progenitors to be roughly consistent with both the observed neutron star birth spin periods and, unlike the Tayler-Spruit dynamo, the core rotation rates of red giants. It cannot, however, explain the rotation rates of intermediate mass stars (den Hartogh et al. 2020). As an alternative solution that does not rely on magnetic torques, many studies have investigated angular momentum transport by internal gravity waves (IGWs) in low- and high-mass stars during various evolutionary phases (e.g., Zahn et al. 1997; Kumar et al. 1999; Talon & Charbonnel 2003; Charbonnel & Talon 2005; Rogers & Glatzmaier 2006; Fuller et al. 2014; Belkacem et al. 2015; Pinçon et al. 2016, 2017) and suggested that IGWs can maintain strong core-envelope coupling only up to the sub-giant branch.

Angular momentum transport by IGWs could, however, again play an important role during more advanced burning stages in massive stars because the enormous convective luminosities and relatively high Mach numbers lead to a strong excitation of IGWs at convective boundaries (Fuller et al. 2015). The familiar wave filtering mechanism for prograde/retrograde modes could then effectively limit the degree of differential rotation in the interior and spin down the core on rather short time scales if rotation is fast to begin with (Fuller et al. 2015). They find that for initially rapidly rotating progenitors, angular momentum transport via g -modes is not efficient enough to explain the pulsar population. They find a maximum spin frequency bound from spin-down of ~ 3 ms, which is consistent with the range of possible birth spins for the fastest spinning solitary pulsar (Marshall et al. 1998, spin period of 16 milliseconds today). Additionally, Fuller et al. (2015), pointed out that IGWs could lead to a stochastic core *spin-up* in initially non-spinning progenitors. The idea here is that stochastically excited IGWs from the convective boundaries of the Si, O, or C shell propagate into the core, where they break and deposit their randomly varying angular momentum. The core angular momentum executes a random walk, as long as there is an influx of IGWs from strong burning shells. In principle, IGWs can also be excited by core convection or shells that end up in the core, and carry angular momentum *outwards*. This mirror process was found to be subdominant in the case studied by Fuller et al. (2015), however.

Fuller et al. (2015) argue that this stochastic spin-up will result in typical neutron birth periods scattering over a range between about 40 ms up to an effective upper limit of ~ 500 ms without the need to assume any progenitor rotation. If the core angular momentum is indeed determined by this stochastic spin-up process, this could explain the paucity of long spin periods of $\gtrsim 500$ ms among young neutron star. Aside from the implications for neutron star spin periods, the excitation of IGWs during the late convective burning stages is also of interest because it could drive mass loss in supernova progenitors shortly before collapse (Quataert & Shiode 2012; Fuller 2017) or lead to envelope inflation (Mcleay & Soker 2014). This could explain observations of circumstellar material (CSM) from late pre-collapse

outbursts in a significant number of observed supernovae (for an overview, see Foley et al. 2011; Smith 2014; Bilinski et al. 2015; Smith 2017), although other mechanisms such as flashes from degenerate shell burning (Woosley & Heger 2015) or the pulsational pair instability (Woosley et al. 2007) may be required to account for more spectacular cases with several solar masses of CSM in Type II_n supernovae.

In this paper, we further investigate the excitation of IGWs during late-stage convective burning and its implication for stochastic core spin-up. Different from the problem of wave excitation by convection during early evolutionary stages, this problem cannot be addressed by asteroseismic measurements. The extant studies of Quataert & Shiode (2012); Fuller et al. (2015); Fuller (2017) strongly rely on the analytic theory of wave excitation by turbulent convection that has been developed over decades (Lighthill 1952; Townsend 1966; Goldreich & Kumar 1990; Quataert & Leconte 2013). Numerical simulations of IGW excitation at convective boundaries have been conducted for earlier evolutionary stages in 2D (Rogers et al. 2013) and 3D (Alvan et al. 2014, 2015; Edelmann et al. 2019), but cannot be easily extrapolated to the late, neutrino-cooled burning stages where the Péclet number is lower and compressibility effects play a bigger role. During the early evolutionary stages, asteroseismology can be used to directly test the underlying theories for IGW excitation by convection (Aerts & Rogers 2015; Aerts et al. 2017). On the other hand, a number of studies have already addressed the late burning stages in 3D (e.g., Meakin & Arnett 2007; Arnett et al. 2008; Müller et al. 2016; Jones et al. 2017; Cristini et al. 2017; Andrassy et al. 2020; Müller et al. 2019; Yadav et al. 2020), but without addressing the problem of stochastic spin-up.

In this study, we use a full 4π -3D numerical simulation to quantitatively study the idea of stochastic spin-up for the first time. We consider a $3M_{\odot}$ He star model from Müller et al. (2019), which we evolved for 7.8 minutes, or ~ 35 convective turnover times. We consider the excitation of waves by vigorous convection in the oxygen burning shell of this model to check the assumptions underlying the theory of Fuller et al. (2015, F15 henceforth) for stochastic core spin-up. We focus on the outward flux of angular momentum from the oxygen shell since wave excitation at the outer boundaries of a convective shell or core is more tractable from the numerical point of view than the excitation of inward-propagating waves from the inner boundary of a convective shell. Since the physical process of wave excitation is the same, this approach nonetheless allows us to study the process in the relevant physical regime and check the scaling relations and dimensionless parameters used in the theory of F15.

The paper is structured as follows: In Section 2, we review key elements of the theory of F15 for the stochastic spin-up of supernova progenitor cores by IGWs. In Section 3 we describe the 3D progenitor model. In Section 4 we analyze the simulation using spherical Favre decomposition to determine the energy and angular momentum flux in convectively stable zones. We compare these results with the random walk model of Fuller et al. (2015), and finally comment on the implications of our results for neutron star birth spins. In Section 5 we discuss potential numerical issues that may affect our results, such as numerical angular momentum

conservation errors, and then summarise our findings in Section 6.

2 THEORY OF STOCHASTIC SPIN-UP

Gravity waves (g -modes) are generated by turbulent convection at convective boundaries, and propagate in the neighboring convectively stable regions. The theory of F15 relies on a few key assumptions about the wave excitation process to model the stochastic spin-up of the core in non-rotating or slowly rotating progenitors.

The first of these assumptions concerns the (time-averaged) IGW energy flux \dot{E} in the stable regions. Following established analytic theory for g -mode excitation (Lighthill 1952; Townsend 1966; Goldreich & Kumar 1990; Quataert & Lecoanet 2013), F15 assume that the wave energy flux \dot{E} depends on the convective luminosity L_{conv} in the driving motions and the convective Mach number \mathcal{M} ,

$$\dot{E} = L_{\text{conv}} \mathcal{M}^\alpha, \quad (1)$$

where the power-law exponent α is expected to lie in the range $\alpha = 5/8-1$.

While the wave energy flux can be assumed to vary only mildly in time, the overshooting convective plumes will continuously excite different modes, and the overall angular momentum flux $\dot{\mathbf{J}}$ carried by the waves will fluctuate according to the wave numbers of the excited modes. F15 assume that the direction of the angular momentum flux vector remains correlated over roughly one convective turnover time τ and varies randomly on longer time scales, so that time-integrated spin-up $\Delta \mathbf{J} = \int \dot{\mathbf{J}} dt$ can be approximated as the result of a random walk by the typical angular momentum δJ of a correlated wave packet per time τ . Thus, after \mathcal{N} convective turnover times, the expectation value $\langle \Delta J^2 \rangle$ is¹

$$\langle \Delta J^2 \rangle = \mathcal{N} \delta J^2. \quad (2)$$

At this stage, one still needs to specify the typical angular momentum δJ carried by one correlated wave packet. For a single mode of spherical harmonics degree ℓ and order m , the z -component \dot{J}_z of the flux of angular momentum is related to the wave energy flux as (Zahn et al. 1997; Kumar et al. 1999),

$$\dot{J}_z = \frac{m}{\omega} \dot{E}, \quad (3)$$

where ω is the mode frequency. F15 suggest replacing m and ω by appropriate averages \bar{m} and $\bar{\omega}$ for the wave packet so that

$$\dot{J}_{\text{F15}} = \frac{\bar{m}}{\bar{\omega}} \dot{E} = \frac{\bar{m}}{\bar{\omega}} \mathcal{M}^\alpha L_{\text{conv}}. \quad (4)$$

They argue that the excited modes will predominantly have periods of the order of the convective turnover time so that $\bar{\omega} = 2\pi/\tau$. For the average wave number, F15 choose $\bar{m} = 1$, arguing that this is the most conservative estimate provided that each wave packet consists only of modes of positive or

negative m . We shall revisit this assumption later in Section 4.

Integrating over one turnover time and using Equation (1), one then finds

$$\delta J_{\text{F15}} = \frac{\bar{m} \tau^2 \dot{J}_{\text{F15}}}{2\pi} = \frac{\tau^2 \mathcal{M}^\alpha L_{\text{conv}}}{2\pi}, \quad (5)$$

and the expected spin-up after \mathcal{N} turnovers is

$$\langle \Delta J_{\text{F15}}^2 \rangle^{1/2} = \sqrt{\mathcal{N}} \delta J_{\text{F15}} = \frac{\sqrt{\mathcal{N}} \bar{m} \tau^2 \dot{J}_{\text{F15}}}{2\pi\sqrt{3}} = \frac{\sqrt{\mathcal{N}} \bar{m} \tau^2 \mathcal{M}^\alpha L_{\text{conv}}}{2\pi\sqrt{3}}, \quad (6)$$

where the factor $1/\sqrt{3}$ accounts for the random orientation of the vectorial angular momentum carried by different wave packets.

3 SHELL BURNING SIMULATION

The challenge is now to determine whether the key approximations in Equations (1), (4), and (6) are borne out by full 3D simulations. We analyse a 3D model of convective shell burning in a non-rotating $3M_\odot$ helium star from Müller et al. (2019). Following the methodology of Müller et al. (2016), we map the underlying 1D stellar evolution model from the KEPLER code (Weaver et al. 1978; Heger & Woosley 2010) into the finite-volume code PROMETHEUS (Fryxell et al. 1989, 1991) at a late pre-collapse stage about 8 minutes before the onset of collapse. Our simulation includes the mass shells initially located between 2,420 km and 16,500 km, which covers three distinct convective zones as illustrated (in turquoise) by the progenitor entropy profile in Figure 1a. Initially there are three convective burning zones: (I), (II) and (III), which are oxygen, neon, and carbon shells respectively. The neon burning region (II) is consumed before collapse and is so thin that g -modes will in fact be able to propagate through it for much of the simulation. By 344 s (5.77 minutes) region (II) has disappeared completely, and there is just one convectively stable region between (I) and (III), shown in Figure 1b. The inner boundary of the grid is contracted in accordance with the mass shell trajectory from the 1D KEPLER model. We use uniform spacing in $\log r$ for the radial coordinate and the axis-free overset Yin-Yang grid (Kageyama & Sato 2004) as implemented by Melson et al. (2015) to cover the full sphere. The grid resolution is $400 \times 56 \times 148$ zones in radius r , latitude θ , and longitude φ on each of the Yin-Yang patches, which corresponds to an angular resolution of 2° . Extremum-preserving 6th-order PPM reconstruction has been implemented in PROMETHEUS following Colella & Sekora (2008).

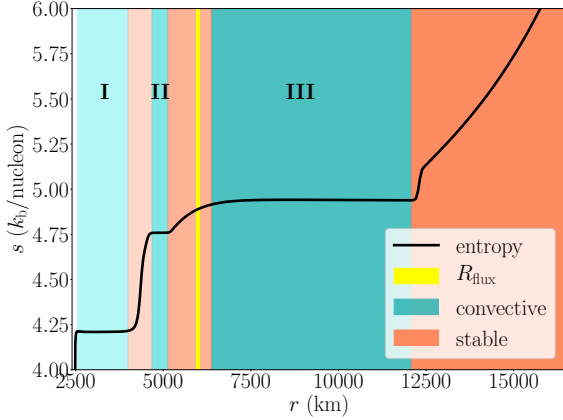
4 RESULTS

4.1 Visual identification of excited modes

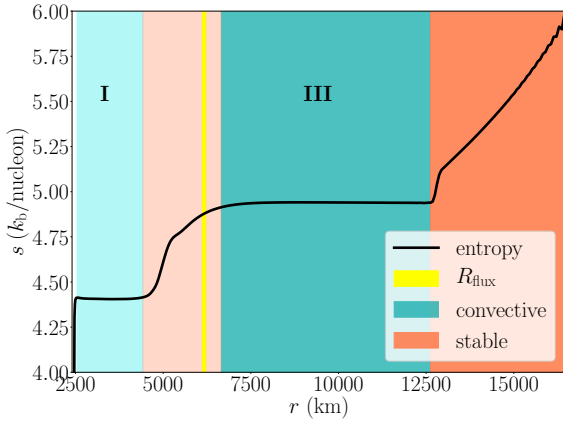
We run the model for 7.8 minutes during oxygen burning. It takes about one minute for convection to fully develop in region (I) from the 1D initial conditions, so we only consider the phase *after* the first minute in our subsequent analysis.

In Figure 2 we show 2D slices of the absolute radial velocity $|v_r|$ and specific entropy s . We have restricted the

¹ Properly speaking, each component ΔJ_i will execute an independent random walk with step size $\delta J_i = \delta J/\sqrt{3}$ if the angular momentum of the wave packets is randomly oriented, but the factor $1/\sqrt{3}$ cancels again when we consider the expectation value of ΔJ^2 since $\langle \Delta J^2 \rangle = 3\langle \Delta J_i^2 \rangle$.



(a) Shell structure at early times.



(b) Shell structure at late times, after the thin neon burning region (II) has disappeared.

Figure 1. Spherically averaged profiles of the specific entropy s (solid black), against our defined regions at early ($t = 144$ s) and late ($t = 368$ s) times. Convective (turquoise) and convectively stable (coral) regions are labelled (I)–(III), with increasing darkness from the inner boundary to the outer boundary. Turbulent fluxes between the convective regions (I) and (III) are evaluated at the radius $R_{\text{flux}} = R_{m=1.65M_{\odot}}$, which is in the convectively stable region between zones (II) and (III) up until around 400 s. The second convective region disappears completely at 344 s; the shell structure after the disappearance of region (II) is shown in Figure 1b.

logarithmic velocity scale to $5\text{--}620 \text{ km s}^{-1}$ to show both the convective motions in region (I) and the excited waves in the surrounding stable region. The boundary between region (I) and the stable region is clearly identifiable in the entropy plot as a relatively sharp discontinuity at a radius of about 4000 km; it is evident that the convective plumes do not overshoot strongly into the stable regions. This clearly identifies the slower, laminar motions of a few 10 km s^{-1} as excited modes. The excited modes are of moderately high wave number and clearly not dominated by dipole or quadrupole modes.

4.2 Expected IGW frequencies

We compute the Brunt–Väisälä frequency ω_{BV} in the convectively stable regions using

$$\omega_{\text{BV}}^2 = g \left(\frac{1}{\Gamma} \frac{d \ln P}{dr} - \frac{d \ln \rho}{dr} \right), \quad (7)$$

where g is the local gravitational acceleration

$$g(r) = \frac{GM(r)}{r^2}, \quad (8)$$

and Γ is the adiabatic exponent $\Gamma = (\partial \ln P / \partial \ln \rho)_s = \rho / P c_s^2$ in terms of the sound speed c_s , the pressure P , and the density ρ at radius r . In Figure 3 we plot $f_{\text{BV}} = \omega_{\text{BV}} / 2\pi$ for the simulated region as a function radius at a late time of 368 s (same time as Figure 1b). In the first convectively stable region, f_{BV} peaks between 0.1–0.4 Hz during the whole simulation. After about 350 s it stays at ~ 0.1 Hz. Waves with frequencies lower than these may propagate as gravity waves in this region. Convective and convectively stable regions (defined by the entropy gradient of Figure 1b) at this time step are included with the same colour scheme as Figure 1. The expected mode frequencies are of a similar order as the convective turnover frequency, and hence the conditions for IGW excitation by convective motions should be close to optimal.

Note that, strictly speaking, the Brunt–Väisälä frequencies computed with Equation (7) are only valid in the linear approximation, where the runaway (convectively unstable) or oscillation (convectively stable) of a stochastically displaced fluid parcel is determined by the local buoyancy excess upon displacement. The fact that there are real Brunt–Väisälä frequencies outside of our convectively stable regions (defined by the entropy gradient) can be explained by the deceleration of fluid parcels as they approach the boundary, where they can penetrate (overshoot) it (see Mocák et al. 2008 for a detailed explanation).

4.3 Angular momentum flux in excited waves

In order to quantify the energy and angular momentum flux carried by the waves excited a convective boundaries, we make use of a spherical Reynolds/Favre decomposition of the flow (Favre 1965). We use hats (or, alternatively, angled brackets) and primes for the volume-weighted Reynolds averages and fluctuating components of extensive quantities such as the density ρ and pressure P (e.g., $\hat{\rho}$ and ρ'). These are defined for any such quantity X as

$$\hat{X}(r) = \langle X \rangle = \int X d\Omega, \quad (9)$$

$$X'(r, \theta, \varphi) = X - \hat{X}(r). \quad (10)$$

Mass-weighted Favre averages and fluctuating components of intensive quantities like the internal energy density ϵ are denoted by tildes and double primes (e.g., $\tilde{\epsilon}$, and ϵ''). For any such quantity Y , we have

$$\tilde{Y}(r) = \frac{\int \rho Y d\Omega}{\int \rho d\Omega}, \quad (11)$$

$$Y''(r, \theta, \varphi) = Y - \tilde{Y}(r). \quad (12)$$

Disregarding subdominant terms for the work done

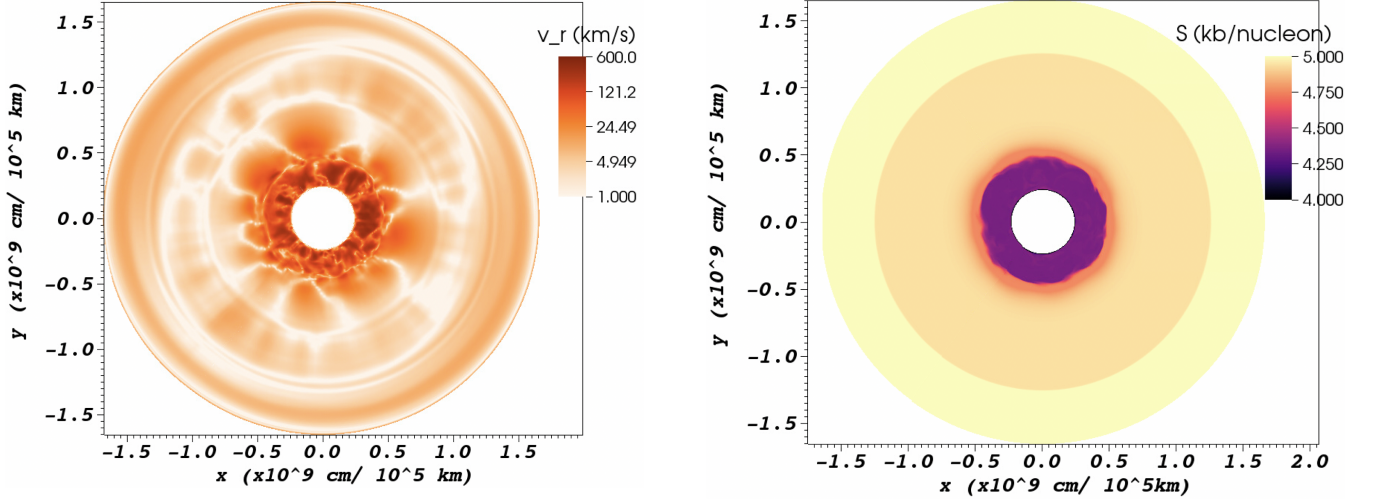


Figure 2. 2D slices showing the absolute value $|v_r|$ of the radial velocity in km s^{-1} (left) and the entropy in $k_b/\text{nucleon}$ (right) at a time of 327 s. In region (I) we find turbulent motions of high velocity. In the surrounding stable region outside $r \approx 4000$ km, we find coherent flow patterns dominated by moderately high multipoles, which is indicative of g -mode activity.

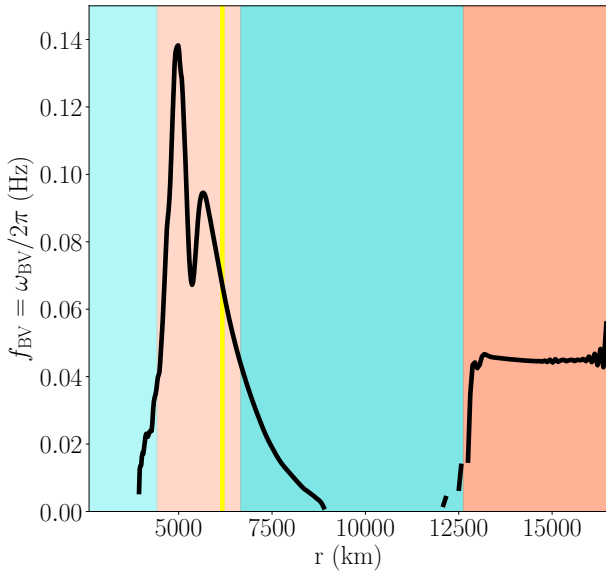


Figure 3. Brunt-Väisälä frequency ω_{BV} as a function of radius r at 368 s (same as Figure 1b), after the middle convective region has disappeared. Based on this profile, gravity waves may propagate in the coral convectively stable zones at frequencies below ~ 0.1 Hz.

by turbulent Reynolds stresses, the Favre-averaged energy equation reads (Müller 2019),

$$\begin{aligned} \frac{\partial}{\partial t} \left(\hat{\rho} \tilde{e} + \hat{\rho} \frac{|\tilde{\mathbf{v}}|^2}{2} + \hat{\rho} \frac{|\langle \tilde{\mathbf{v}}'' \rangle|^2}{2} \right) + \nabla \cdot \left[\left(\hat{\rho} \tilde{e} + \hat{\rho} \frac{|\tilde{\mathbf{v}}|^2}{2} + \hat{P} \right) \tilde{\mathbf{v}} \right] \\ + \nabla \cdot \left[\langle \hat{\rho} \tilde{e}'' \mathbf{v}'' \rangle + \langle P' \mathbf{v}'' \rangle + \langle \rho \mathbf{v}'' \frac{|\mathbf{v}''|^2}{2} \rangle \right] = 0. \end{aligned} \quad (13)$$

The relevant terms containing the energy flux carried by waves excited at convective boundaries are the convective energy flux $\mathbf{F}_{\text{conv}} = \langle \hat{\rho} \tilde{e}'' \mathbf{v}'' \rangle$ (for the turbulent transport of internal energy), the “acoustic” energy flux $\mathbf{F}_{\text{sound}} = \langle P' \mathbf{v}'' \rangle$, and the turbulent kinetic energy flux $\mathbf{F}_{\text{kin}} = \langle \rho \mathbf{v}'' \frac{|\mathbf{v}''|^2}{2} \rangle$.

Strictly speaking, however, one can only properly separate the flux carried by gravity waves and acoustic waves using a decomposition of the fluctuating components into eigenmodes. When using the Favre decomposition of the energy equation, the wave energy flux is split between the three turbulent flux components. At the same time acoustic waves and entrainment contribute to the turbulent fluxes, which is particularly problematic in the case of entrainment, which produces a *negative* energy flux near the convective boundary.

Due to these difficulties in isolating the wave energy flux \dot{E} from region (I), we do not test Equation (1), for which there is strong justification from theory and simulations anyway (Goldreich & Kumar 1990; Quataert & Lecoanet 2013; Pinçon et al. 2016). Instead, we assume $\dot{E} = \mathcal{M} L_{\text{conv}}$, and directly test the dependence of \dot{J} on L_{conv} and \mathcal{M} in Equation (4).

To obtain \dot{J} , we consider the Favre-averaged equation for the transport of angular momentum, which only contains two flux terms \mathbf{F}_{adv} and \mathbf{F}_{turb} for the mean (advective) and turbulent angular momentum flux,

$$\frac{\partial \langle \rho l \rangle}{\partial t} + \nabla \cdot \mathbf{F}_{\text{adv}} + \nabla \cdot \mathbf{F}_{\text{turb}} = 0, \quad (14)$$

where

$$\mathbf{F}_{\text{turb}} = \langle \rho l'' u_r'' \rangle, \quad (15)$$

and

$$\mathbf{F}_{\text{adv}} = \langle \rho \tilde{l} \tilde{u}_r \rangle = \rho \tilde{l} \tilde{u}_r. \quad (16)$$

For a full derivation, we refer to Appendix A. For our purpose, only the turbulent angular momentum flux \mathbf{F}_{turb} is of interest, which contains the flux carried by gravity waves and

acoustic waves. We evaluate the angular momentum flux out of region (I) at a fixed mass coordinate of $m = 1.65M_{\odot}$. We choose a fixed mass shell rather than a fixed radius because this mass shell stays inside the convectively stable region until around 400 s; a fixed analysis radius would be problematic because of the contraction of the shells during the simulation.

Using the numerically computed turbulent angular momentum flux, we can now proceed to assess Equation (4). To evaluate the right-hand side (RHS) of Equation (1), we use the maximum of the ratio of RMS velocity fluctuation v_r'' to the sound speed c_s in the convectively stable region containing R_{flux} ,

$$\mathcal{M} = \max_{\text{I}} \left(\frac{(\widetilde{v_r''})^{1/2}}{\tilde{c}_s} \right), \quad (17)$$

and use the volume-integrated nuclear energy generation rate \dot{Q}_{nuc} in region (I) as a proxy for the convective luminosity L_{conv} , which is well justified under steady state conditions (Arnett et al. 2008; Müller et al. 2016)². Finally, we need the convective turnover time to evaluate Equation (4), which is computed from the width of the convective region (I) and the maximum convective velocity fluctuation v_r'' ,

$$\tau = \Delta r / \max_{\text{I}} (v_r''). \quad (18)$$

In Figure 4, we plot the ratio of the turbulent angular momentum flux $\dot{J} = 4\pi r^2 |\mathbf{F}_{\text{turb}}|$ to the value $\dot{J}_{\text{F15}} = \tau \mathcal{M} L_{\text{conv}} / (2\pi)$ predicted by F15. Once convection in region (I) has reached a steady state, the angular momentum flux \dot{J} only reaches a fraction of a few $\sim 10^{-2}$ of the flux predicted by F15. If we accept the scaling $\dot{E} = \mathcal{M}^{\alpha} L_{\text{conv}}$ for the wave energy flux, this result implies that the effective average wave number of the excited wave packets must be *much smaller* than $\bar{m} = 1$ despite the fact that the excited modes have rather *high* angular wave numbers as discussed in Section 4.1.³ It is, in fact, natural to expect that $\bar{m} = 1$ is not a lower bound for the average wave number if one considers the dynamics of wave excitation at convective boundaries. Convective plumes are driven by radial buoyancy forces and therefore hit the convective boundary almost perpendicularly. Any overshooting plume will therefore tend to launch gravity waves propagating in all directions away from the plume (i.e., with wave numbers of opposing sign) with similar amplitude. A small asymmetry between modes of different m can still arise if the plume wanders around, but the convective updrafts and downdrafts tend to be rather stationary in simulations of convection during the neutrino-cooled burning stages, and hence there is only a small asymmetry in amplitude between excited modes of opposite m . Contrary to the assumption of F15, $\bar{m} = 1$ is therefore not a strict lower bound for a single wave packet launched by

² One could also define L_{conv} as the maximum of the turbulent energy flux \dot{E} inside a convective region. This yields similar, but more noisy results.

³ Alternatively, one might surmise that the excited modes have frequencies higher than $\omega = 2\pi/\tau$, but unless there is resonant excitation it is unavoidable that the frequency spectrum of the excited modes roughly reflects the frequency spectrum of the turbulent driving motions.

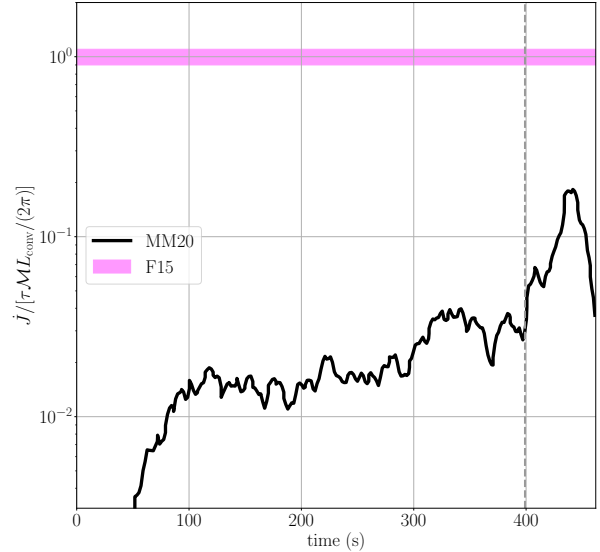


Figure 4. Ratio of the turbulent angular momentum flux $\dot{J} = |\mathbf{F}_{\text{turb}}|$ from our 3D simulation (MM20) to the prediction from Equation (4), based on our calculations of the convective Mach number \mathcal{M} and convective burning luminosity \dot{Q}_{nuc} (and hence the energy flux via Equation (1)) and convective turnover frequency. Our computed angular momentum flux is smaller by a factor of $\sim 10^2$ than what the model in F15 suggests when using the typical wave number $\bar{m} = 1$. After around 400 s (grey dashed line), the mass coordinate where we measure the angular momentum flux resides *inside* the inner convective region (I), so the ratio is no longer reliable.

an overshooting plume; $\bar{m} < 1$ is easily possible and in fact expected for waves excited by buoyancy-driven convection.

4.4 Testing the Random Walk Assumption

The relatively small values of the turbulent angular momentum flux already indicate that the mechanism for stochastic spin-up is considerably less efficient than F15 estimated. However, there is yet another potential problem that could further reduce the efficiency of stochastic spin-up. One might suspect that the excitation of modes by overshooting plumes is not a time-independent stochastic process that results in a random walk of the angular momentum of the convective region that launches the waves, and of the angular momentum in the destination region. Instead, there could be a regression to zero if the stochastic excitation were to predominantly produce prograde modes, which would drive the angular momentum of the driving region towards zero. Such a mechanism could operate independently of the familiar filtering mechanism for prograde and retrograde modes and limit stochastic fluctuations of the angular momentum of convective shells even when there is no strong differential rotation.

In order to determine whether there is such a restoring mechanism, or whether the random walk assumption of F15 is valid, we first need to generalise Equation (6) to accom-

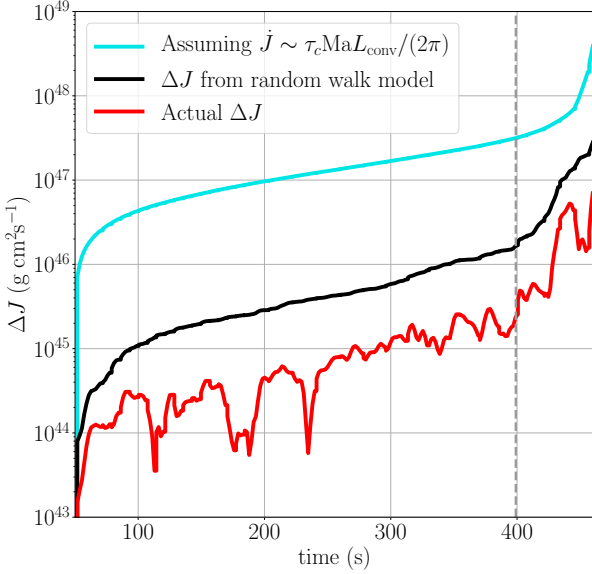


Figure 5. The change in angular momentum, ΔJ , inside the mass coordinate $m = 1.65M_{\odot}$ based on the three different formulations of ΔJ in Equations (19), (20), and (21). The angular momentum computed from the simulation (Equation 20) is in red and the angular momentum computed assuming a random walk via Equation (19) is in black. The angular momentum calculated from Equation (21) assuming the relation (4) between the angular momentum flux and the convective luminosity is in cyan. After 400 s (dashed grey line) the mass coordinate where we measure the flux lies inside the convective region (I) (see Figure 1). The significant growth of ΔJ in the last 70 s is the result of stochastic angular momentum redistribution *inside* the convective zone, and not associated with a flux of IGWs. The wave packet random walk model is no longer applicable during this phase and cannot be used to infer spin-up of the region from IGWs.

modate the slow, secular changes in convective luminosity and turnover time as the oxygen burning shell contracts. We can then compare the actual time-integrated angular momentum flux to this generalised random walk model. It is straightforward to determine the root-mean-square expectation value ΔJ_{RW} for a continuous random walk process by integrating the variance of each angular momentum component $\delta J_i^2 = (\tau \dot{J}_i)^2 = |\tau \dot{J}|^2 / 3$ of each wave packet times the assumed correlation frequency of the random walk process (i.e. the convective turnover frequency τ^{-1} in the model of F15),

$$\Delta J_{\text{RW}}(t) = \left[\sum_{i=1}^3 \int_0^t (\delta J_i)^2 \frac{dt'}{\tau} \right]^{1/2} = \left[\sum_{i=1}^3 \int_0^t \tau \dot{J}_i(t')^2 dt' \right]^{1/2}. \quad (19)$$

Figure 5 compares ΔJ_{RW} (in black) to the actual time-integrated angular momentum flux (in red) ΔJ ,

$$\Delta J(t) = \left[\sum_{i=1}^3 \left(\int_0^t \dot{J}_i(t') dt' \right)^2 \right]^{1/2}. \quad (20)$$

For illustrative purposes, we also show the predicted spin-

up $\Delta J_{\text{F15}}(t)$ for the original random walk model of F15 with $\dot{J} = \dot{E}\tau/2\pi$ (i.e. $\bar{m} = 1$) and $\dot{E} = ML_{\text{conv}}$ in cyan,

$$\Delta J_{\text{F15}}(t) = \frac{1}{\sqrt{3}} \left[\int_0^t \tau^{-1} \left(\frac{\tau^2 ML_{\text{conv}}}{2\pi} \right)^2 dt' \right]^{1/2}. \quad (21)$$

Interestingly, even though ΔJ_{RW} (black) still overpredicts the actual time-integrated angular momentum flux ΔJ (red) by a factor of 5 on average, this is not a huge discrepancy. The growth of ΔJ appears roughly compatible with a random walk, only with an effective correlation time that is 4% of what is assumed in F15, since the spin-up scales with the square root of the correlation time, $\Delta J_{\text{RW}} \propto \sqrt{\tau}$. This short correlation time may be related to the rather high wave numbers of the excited modes. The effective correlation time of the random walk must reflect the characteristic time scale of the forcing motions with similar wave numbers, or in other words, of relatively small-scale structures in the convective flow, which evolve on significantly shorter time scales than τ_{conv} .

Thus, our simulation actually *supports* the assumption that stochastic wave excitation will lead to the core angular momentum executing a random walk, albeit with a shorter correlation time. However, because the assumption of $\bar{m} = 1$ is not valid and because the correlation time of the random walk is somewhat shorter than the convective turnover time in our simulations, the original model of F15 overpredicts ΔJ by several orders of magnitude.

On the other hand, Figure 5 suggests that the late convective burning stages might stochastically affect the remnant angular momentum in a different manner. During the last 70 s of the simulation, the analysis radius lies *inside* the oxygen shell, and the measured ΔJ indicates stochastic *internal* redistribution of angular momentum within the shell. This stochastic redistribution of angular momentum could potentially spin-up the inner regions of the shell considerably. In the present example, the time-integrated flux of angular momentum ΔJ *within* the oxygen shell during the last 70 s is ten times bigger than the time-integrated wave-mediated flux of angular momentum out of the oxygen shell. If only part of the oxygen shell is ejected during the supernova explosion, the total angular momentum within the “mass cut” may be considerable. If the mass cut were placed at $1.65M_{\odot}$ (which is much larger than is realistic for this model, cp. Müller et al. 2019), the resulting neutron star spin period would be of order 100 ms. Naturally, the theory of stochastic IGW excitation cannot be applied to stochastic variations within convective regions close to the mass cut, so one cannot make generic predictions about the importance of this phenomenon. However, 3D supernova progenitor models that include this effect naturally anyway are becoming more widely used.

4.5 Estimate of neutron star spin periods

Figure 5 shows that during the simulation time of about 7 minutes, the angular momentum transported out of the oxygen shell from the outer boundary is about $2 \times 10^{45} \text{ g cm}^2 \text{ s}^{-1}$. If a similar amount of angular momentum is transported inwards into the core, and the angular momentum is conserved during the collapse to a neutron star, this would result in a neutron star rotation rate $\omega \approx 1 \text{ rad s}^{-1}$ of

a typical neutron star moment of inertia $\sim 1.5 \times 10^{45} \text{ g cm}^2$. However, our simulation only covers the last phase in the life of the second oxygen shell. To gauge the actual impact of stochastic spin-up, we need to extrapolate our results to the entire lifetime of a shell similar to F15, but with different efficiency factors.

For this purpose, it is convenient to express all relevant quantities in Equation (6) in terms of the shell mass ΔM , inner radius R and width ΔR , the average Q -value of the nuclear reaction per unit mass, q , and the nuclear time scale τ_{nuc} for the respective burning phase. Using $L_{\text{conv}} = \Delta M q / \tau_{\text{nuc}}$, we find the convective velocity from mixing-length theory as calibrated against 3D simulations (Müller et al. 2016),

$$v_{\text{conv}} = \frac{1}{2} \left(\frac{L_{\text{conv}} h_P}{m} \right)^{1/3} = \frac{1}{2} \left(\frac{qR/4}{\tau_{\text{nuc}}} \right)^{1/3}, \quad (22)$$

where we have taken the pressure scale height to be $h_P = P/(\rho g) \approx R/4$, which is a good approximation during advanced burning stages in massive stars. The sound speed at the bottom of the shell is approximately

$$c_s = \left(\frac{GM}{3R} \right)^{1/2}, \quad (23)$$

so that we can write the convective Mach number as

$$\mathcal{M} = \frac{v_{\text{conv}}}{c_s} = \frac{1}{2} \left(\frac{qR}{4\tau_{\text{nuc}}} \right)^{1/3} \left(\frac{GM}{3R} \right)^{-1/2}, \quad (24)$$

and find the convective turnover time to be $\tau_{\text{conv}} = \Delta R / v_{\text{conv}}$. Putting all this together in Equation (6) and noting that we have $\mathcal{N} = \tau_{\text{nuc}} / \tau_{\text{conv}}$ turnovers over the lifetime of the shell, we find

$$\begin{aligned} \Delta J &= \frac{\alpha}{\sqrt{3}} \sqrt{\frac{\tau_{\text{nuc}}}{\tau_{\text{conv}}}} \left(\frac{\tau_{\text{conv}}^2 \mathcal{M} \Delta M q}{2\pi \tau_{\text{nuc}}} \right) \\ &\approx 3.4 \times 10^{-3} \times \frac{\Delta R^{3/2} \Delta M q^{5/6} R^{1/3}}{\sqrt{G} \sqrt{M} \tau_{\text{nuc}}^{1/3}}, \end{aligned} \quad (25)$$

where we have replaced the average wave number \bar{m} in Equation (6) with an efficiency factor $\alpha \sim 10^{-2}$ in line with our simulation results. This can be used for any of the neutrino-cooled shell burning phases, but as pointed out by F15, one expects the last shell burning stage to determine the stochastic spin-up at the time of collapse because deterministic angular momentum transport can spin down the core again if the shell is extinguished before collapse. Typically, this will be the second or third oxygen shell (Collins et al. 2018), though in some cases, the most violent active shell at or close before collapse is the silicon shell as assumed by F15. Since the last oxygen shell typically has a higher mass, larger radius and width, shorter duration, and a higher average Q -value of $q \approx 0.4 \text{ MeV}/m_u$ than the silicon shell, most of the factors in Equation (25) have slightly more favorable values than used by F15 for silicon shells. With a neutron star moment of inertia $I = 0.36 M R_{\text{NS}}^2$ and a neutron star radius of $R_{\text{NS}} = 12 \text{ km}$, Equation (25) translates into a characteristic spin period of

$$\begin{aligned} P_{\text{NS}} &= 13.5 \text{ s} \times \left(\frac{M}{1.4 M_{\odot}} \right)^{3/2} \times \left(\frac{\Delta M}{0.1 M_{\odot}} \right)^{-1} \times \left(\frac{R}{3000 \text{ km}} \right) \\ &\quad \times \left(\frac{\Delta R}{1000 \text{ km}} \right)^{-3/2} \times \left(\frac{\tau_{\text{nuc}}}{10^4 \text{ s}} \right)^{1/3} \times \left(\frac{q}{0.4 \text{ MeV}/m_u} \right)^{5/6}, \end{aligned} \quad (26)$$

in terms of typical parameters for oxygen shells in low-mass supernova progenitors. Based on the efficiency parameters in our simulations, we therefore expect stochastic spin-up to play a negligible role in low-mass progenitors compared to stochastic spin-up during the early explosion phase (Wongwathanarat et al. 2013; Müller et al. 2019) and by late-time fallback (Chan et al. 2020; Stockinger et al. 2020), which can achieve spin periods from a few seconds down to milliseconds. For high-mass progenitors with $\Delta M \sim 1 M_{\odot}$ and wider oxygen shells $\Delta R \sim 5000 \text{ km}$, spin periods of order 100 ms remain within reach even with a much lower efficiency factor than assumed by F15, and stochastic spin-up by IGWs might still be a relevant factor in determining the neutron star spin period along with other angular momentum processes during the progenitor evolution and spin-up/spin-down processes during the explosion.

5 EFFECTS OF NUMERICAL CONSERVATION ERRORS

Finite-volume methods as used in PROMETHEUS generally cannot conserve total angular momentum to machine accuracy (unlike smoothed-particle hydrodynamics). Moreover, angular momentum transport in any grid-based or particle-based simulation will be affected to some degree by numerical dissipation. One may justifiably ask whether non-conservation of total angular momentum or numerical dissipation have any bearing on our simulation of stochastic spin-up. In the context of the preceding discussion, it is especially pertinent, whether the convective region (I) is indeed spun up in the opposite direction to the angular momentum that is lost by waves. This specific problem can already be addressed here, though more extensive resolution studies and simulations with different reconstruction and discretisation schemes naturally remain desirable for the future.

As a simple check on the quality of angular momentum conservation in our simulation, we compare the time-integrated angular momentum flux from region (I) to the volume-integrated angular momentum. Unlike when we calculated the angular momentum flux for the random walk at a fixed mass coordinate, we compute the angular momentum dissipation at a fixed radial coordinate, so that we can formulate the angular momentum “budget” for region (I) using Gauss’ theorem. We define the analysis region region C1 as the sphere contained within $r = 4337 \text{ km}$, i.e. the boundary of C1 is in the middle of the convectively stable region between regions (I) and (II) once 3D burning and convection develops. Analytically, we have

$$\int_{C1} \rho \mathbf{l} dV = - \int_0^t \oint_{\partial C1} \rho \mathbf{l} \mathbf{v} \cdot \mathbf{dA} dt'. \quad (27)$$

In Figure 6, we compare the left-hand side and the right-hand side of Equation (27) for the x -, y -, and z -component of the angular momentum. For all three components, at the end of the simulation the direction of the convective shell angular momentum is indeed the opposite sign of the angular momentum leaving at the flux boundary. Early on, the evolution of \mathbf{J} is dominated by numerical errors, the y -component in particular shows a significant drift over the first 200 s. As soon as convection is fully developed and the

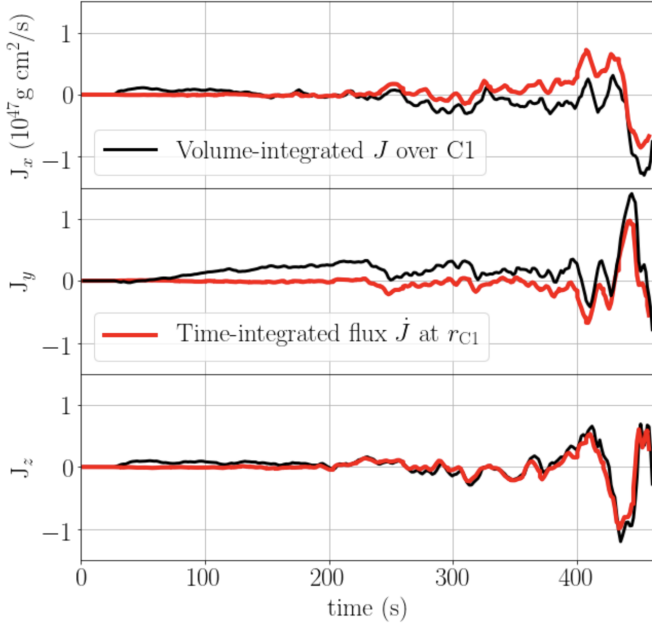


Figure 6. Time-integrated angular momentum flux at the fixed boundary C1 (red) and the (negative) integrated angular momentum over the volume enclosed by C1 (black) in the x , y and z directions. For each component, the angular momentum in the spun-up convective shell volume is consistent with the angular momentum flux leaving the volume.

excited waves from the convective boundary carry a significant angular momentum flux, the evolution of the total angular momentum in the analysis region clearly follows the time-integrated angular momentum flux. This suggests that angular momentum conservation errors do not significantly affect our analysis at times later than ~ 200 s. Of course, more subtle numerical issues, such as artificial damping of the excited waves, may limit the accuracy of our results and need to be further investigated in the future. However, we believe that the key findings of this study will likely remain robust. The code clearly has the ability to evolve relatively weak waves, and the waves that would need to be resolved for the mechanism of F15 to work effectively are not of extremely short wavelength, so that excessive dissipation is likely not a critical problem.

6 CONCLUSIONS

Using the 3D hydrodynamics code PROMETHEUS, we studied the angular momentum flux from stochastically excited IGWs during oxygen shell burning in an initially non-rotating massive star. Our findings allow us to better assess the efficiency of stochastic wave excitation as a process for core spin-up, which has been suggested by Fuller et al. (2015) based on analytic theory.

In agreement with the theory of Fuller et al. (2015), we find that the IGW-mediated flux of angular momentum out of a convective shell in a non- or slowly-rotating progenitor can indeed be described by a random-walk process. However we find that the correlation time of this random-walk process is only a fraction of the convective turnover time and hence significantly shorter than assumed by Fuller et al. (2015).

This reduces the amplitude of the random walk by a factor of several.

We also find a smaller ratio between the angular momentum flux carried by the excited IGWs and the convective luminosity by more than an order of magnitude than assumed by Fuller et al. (2015). We ascribe this discrepancy to the fact that the assumption of an average zonal wave number $\bar{m} = 1$ of individual IGW “wave packets” is too optimistic, since IGWs excited by overshooting convective plumes will generally contain modes with opposite zonal wave number m of almost equal amplitude. Therefore the average zonal wave number \bar{m} of each wave packet will be much smaller than unity and the net angular momentum carried by the wave packet will be very small.

The combination of a shorter effective correlation time and a smaller instantaneous angular momentum flux results in a time-integrated stochastic angular momentum flux from the oxygen shell that is about a factor of $\sim 10^2$ smaller than predicted by the model of Fuller et al. (2015). It should be pointed out, however, that our simulation is compatible with their analytic scaling laws; it merely suggests that the relevant dimensionless parameters of the model may be quite small.

The characteristic spin period from stochastic spin-up of the core by IGWs over the entire life of a convective burning shell can be estimated based on the mass, radius, width, and lifetime of the shell from 1D stellar evolution models using a simple scaling relation (Equation 26). Extrapolating our simulation results over the entire life time of convective shells, we estimate that stochastic spin-up by IGWs alone would result in neutron star birth spin periods of several seconds for low-mass stars and down to ~ 0.1 s for high-mass stars with thick oxygen shells. These spin rates are slower than predicted by Fuller et al. (2015) by one to two orders of magnitude. Thus our findings suggest that stochastic spin-up of progenitor cores will usually not play a major role in determining the core spin rates of massive stars and neutron star birth periods, because stochastic spin-up processes during the supernova explosion will impart more angular momentum onto the neutron star.

It remains to be seen, however, to what extent the efficiency factors for IGW excitation and stochastic core spin-up found in our simulation depend on the detailed properties of convective zones and the structure of the convective boundary. For example, the correlation time of the random walk and the average zonal wave number will depend on the typical size of the convective eddies. Convection zones with pronounced large-scale flow patterns and fewer but stronger plume impact events may provide more favorable conditions for stochastic core spin-up. In future, one should also investigate stiffer convective boundaries with sharp entropy jumps; the inner convective boundaries, which are of highest relevance for the problem of stochastic spin-up, are considerably stiffer than the convective boundary considered in this study. Moreover, the dependence of stochastic spin-up on the convective Mach number should be investigated numerically to confirm the predicted scaling laws. We also note that stochastic angular momentum redistribution *within* convective zones close to the mass cut could be relevant for predicting neutron star birth spin periods. This effect is already implicitly included in modern 3D supernova progenitor models. Better understanding convection, wave excitation, and

angular momentum transport by 3D simulations will remain challenging because of the technical difficulties of low-Mach number flow, stringent resolution requirements at stiff convective boundaries, and the numerical problem of angular momentum conservation. However, 3D simulations of convective burning are clearly proving useful in understanding angular momentum transport processes in supernova progenitors.

ACKNOWLEDGEMENTS

We acknowledge fruitful discussions with A. Heger and I. Mandel. LM acknowledges support by an Australian Government Research Training (RTP) Scholarship. BM has been supported by the Australian Research Council through Future Fellowship FT160100035 and partly as an Associate Investigator of the ARC Centre of Excellence *OzGrav* (CE170100004). This research was undertaken with the assistance of resources from the National Computational Infrastructure (NCI), which is supported by the Australian Government and was supported by resources provided by the Pawsey Supercomputing Centre with funding from the Australian Government and the Government of Western Australia.

REFERENCES

- Aerts C., Rogers T. M., 2015, *ApJ*, **806**, L33
- Aerts C., et al., 2017, *A&A*, **602**, A32
- Alvan L., Brun A. S., Mathis S., 2014, *A&A*, **565**, A42
- Alvan L., Strugarek A., Brun A. S., Mathis S., Garcia R. A., 2015, *A&A*, **581**, A112
- Andrassy R., Herwig F., Woodward P., Ritter C., 2020, *MNRAS*, **491**, 972
- Arnett D., Meakin C., Young P. A., 2008, *The Astrophysical Journal*, **690**, 1715
- Beck P. G., et al., 2012, *Nature*, **481**, 55
- Beck P. G., et al., 2014, *A&A*, **564**, A36
- Belkacem K., et al., 2015, *A&A*, **579**, A31
- Bilinski C., Smith N., Li W., Williams G. G., Zheng W., Filippenko A. V., 2015, *MNRAS*, **450**, 246
- Blondin J. M., Mezzacappa A., 2007, *Nature*, **445**, 58
- Cantiello M., Mankovich C., Bildsten L., Christensen-Dalsgaard J., Paxton B., 2014, *ApJ*, **788**, 93
- Chan C., Müller B., Heger A., 2020, *Monthly Notices of the Royal Astronomical Society*
- Charbonnel C., Talon S., 2005, *Science*, **309**, 2189
- Colella P., Sekora M. D., 2008, *Journal of Computational Physics*, **227**, 7069
- Collins C., Müller B., Heger A., 2018, *MNRAS*, **473**, 1695
- Cristini A., Meakin C., Hirschi R., Arnett D., Georgy C., Viallet M., Walkington I., 2017, *MNRAS*, **471**, 279
- Deheuvels S., et al., 2012, *ApJ*, **756**, 19
- Deheuvels S., et al., 2014, *A&A*, **564**, A27
- Edelmann P. V. F., Ratnasingam R. P., Pedersen M. G., Bowman D. M., Prat V., Rogers T. M., 2019, *ApJ*, **876**, 4
- Faucher-Giguère C.-A., Kaspi V. M., 2006, *ApJ*, **643**, 332
- Favre A. J., 1965, *Journal of Applied Mechanics*, **32**, 241
- Foley R. J., Berger E., Fox O., Levesque E. M., Challis P. J., Ivans I. I., Rhoads J. E., Soderberg A. M., 2011, *ApJ*, **732**, 32
- Fryxell B. A., Müller E., Arnett D., 1989, Max-Planck-Institut für Astrophysik, Preprint0, 449
- Fryxell B., Arnett D., Mueller E., 1991, *ApJ*, **367**, 619
- Fuller J., 2017, *MNRAS*, **470**, 1642
- Fuller J., Lecoanet D., Cantiello M., Brown B., 2014, *The Astrophysical Journal*, **796**, 17
- Fuller J., Cantiello M., Lecoanet D., Quataert E., 2015, *ApJ*, **810**, 101
- Fuller J., Piro A. L., Jermyn A. S., 2019, *MNRAS*, **485**, 3661
- Goldreich P., Kumar P., 1990, *ApJ*, **363**, 694
- Gullón M., Miralles J. A., Viganò D., Pons J. A., 2014, *MNRAS*, **443**, 1891
- Heger A., Woosley S. E., 2010, *ApJ*, **724**, 341
- Heger A., Langer N., Woosley S. E., 2000, *ApJ*, **528**, 368
- Heger A., Woosley S. E., Spruit H. C., 2005, *ApJ*, **626**, 350
- Hirschi R., Meynet G., Maeder A., 2004, *A&A*, **425**, 649
- Jones S., Andrassy R., Sandalski S., Davis A., Woodward P., Herwig F., 2017, *MNRAS*, **465**, 2991
- Kageyama A., Sato T., 2004, *Geochemistry, Geophysics, Geosystems*, **5**, n/a
- Kazeroni R., Guilet J., Foglizzo T., 2016, *MNRAS*, **456**, 126
- Kumar P., Talon S., Zahn J.-P., 1999, *ApJ*, **520**, 859
- Lighthill M. J., 1952, *Proceedings of the Royal Society of London Series A*, **211**, 564
- Marshall F. E., Gotthelf E. V., Zhang W., Middleditch J., Wang Q. D., 1998, *ApJ*, **499**, L179
- Mcley L., Soker N., 2014, *Monthly Notices of the Royal Astronomical Society*, **445**, 2492
- Meakin C. A., Arnett D., 2007, *The Astrophysical Journal*, **667**, 448
- Melson T., Janka H.-T., Marek A., 2015, *ApJ*, **801**, L24
- Mocák M., Müller E., Weiss A., Kifonidis K., 2008, *A&A*, **490**, 265
- Mosser B., et al., 2012, *A&A*, **548**, A10
- Müller B., 2019, *MNRAS*, **487**, 5304
- Müller B., Viallet M., Heger A., Janka H.-T., 2016, *ApJ*, **833**, 124
- Müller B., et al., 2019, *MNRAS*, **484**, 3307
- Noutsos A., Schnitzeler D. H. F. M., Keane E. F., Kramer M., Johnston S., 2013, *MNRAS*, **430**, 2281
- Pinçon C., Belkacem K., Goupil M. J., 2016, *A&A*, **588**, A122
- Pinçon C., Belkacem K., Goupil M. J., Marques J. P., 2017, *A&A*, **605**, A31
- Pope S. B., 2000, *Turbulent Flows*. Cambridge University Press, doi:10.1017/CBO9780511840531
- Popov S. B., Turolla R., 2012, *Monthly Notices of the Royal Astronomical Society: Letters*, **421**, L127
- Popov S. B., Pons J. A., Miralles J. A., Boldin P. A., Posselt B., 2010, *MNRAS*, **401**, 2675
- Quataert E., Lecoanet D., 2013, *Monthly Notices of the Royal Astronomical Society*, **430**, 2363
- Quataert E., Shiode J., 2012, *MNRAS*, **423**, L92
- Rantsiou E., Burrows A., Nordhaus J., Almgren A., 2011, *ApJ*, **732**, 57
- Rogers T. M., Glatzmaier G. A., 2006, *ApJ*, **653**, 756
- Rogers T. M., Lin D. N. C., McElwaine J. N., Lau H. H. B., 2013, *The Astrophysical Journal*, **772**, 21
- Shu F. H., 1992, *Physics of Astrophysics*, Vol. II. University Science Books
- Smith N., 2014, *ARA&A*, **52**, 487
- Smith N., 2017, *Interacting Supernovae: Types IIn and Ibn*. Springer International Publishing, Cham, pp 403–429, doi:10.1007/978-3-319-21846-5_38, https://doi.org/10.1007/978-3-319-21846-5_38
- Spruit H. C., 2002, *A&A*, **381**, 923
- Stockinger G., et al., 2020, arXiv e-prints, p. arXiv:2005.02420
- Suijs M. P. L., Langer N., Poelarends A. J., Yoon S. C., Heger A., Herwig F., 2008, *A&A*, **481**, L87
- Talon S., Charbonnel C., 2003, *A&A*, **405**, 1025
- Theureau G., et al., 2011, *A&A*, **525**, A94
- Townsend A. A., 1966, *Journal of Fluid Mechanics*, **24**, 307
- Weaver T. A., Zimmerman G. B., Woosley S. E., 1978, *ApJ*, **225**, 1021

- Wheeler J. C., Kagan D., Chatzopoulos E., 2015, [ApJ](#), **799**, 85
- Wongwathanarat A., Janka H.-T., Müller E., 2013, [A&A](#), **552**,
[A126](#)
- Woosley S. E., Heger A., 2015, [ApJ](#), **810**, 34
- Woosley S. E., Blinnikov S., Heger A., 2007, [Nature](#), **450**, 390
- Yadav N., Müller B., Janka H. T., Melson T., Heger A., 2020,
[ApJ](#), **890**, 94
- Zahn J. P., Talon S., Matias J., 1997, [A&A](#), **322**, 320
- den Hartogh J. W., Eggenberger P., Deheuvels S., 2020, [A&A](#),
634, L16

APPENDIX A: FAVRE-AVERAGED ANGULAR MOMENTUM TRANSPORT EQUATION

To derive the Favre-averaged angular momentum transport equation, we cross \mathbf{r} with the momentum equation (Shu 1992; Pope 2000),

$$\mathbf{r} \times \left[\frac{\partial(\rho\mathbf{u})}{\partial t} + \nabla \cdot (\rho\mathbf{u} \otimes \mathbf{u}) \right] \nabla P + = \mathbf{r} \times \rho\mathbf{g}. \quad (\text{A1})$$

It is convenient to write this in component form as,

$$\frac{\partial(\epsilon_{ijk}r_j\rho u_k)}{\partial t} + \epsilon_{ijk}r_j\nabla_l(\rho u_l u_k + \delta_{lk}P) = \epsilon_{ijk}r_j\rho g_k, \quad (\text{A2})$$

which leads to

$$\frac{\partial(\epsilon_{ijk}r_j\rho u_k)}{\partial t} + \nabla_l[\epsilon_{ijk}r_j(\rho u_l u_k + P\delta_{lk})] - \epsilon_{ijk}(\rho u_l u_k + P\delta_{lk}) \underbrace{\nabla_l r_j}_{=\delta_{lj}} = \epsilon_{ijk}r_j\rho g_k, \quad (\text{A3})$$

and hence

$$\frac{\partial(\epsilon_{ijk}r_j\rho u_k)}{\partial t} + \nabla_l[\epsilon_{ijk}r_j(\rho u_l u_k + P\delta_{lk})] - \underbrace{\epsilon_{ijk}(\rho u_j u_k + P\delta_{lk})}_{=0} = \epsilon_{ijk}r_j\rho g_k. \quad (\text{A4})$$

This can again be written in component-free notation

$$\frac{\partial\rho\mathbf{l}}{\partial t} + \nabla \cdot (\rho\mathbf{u} \otimes \mathbf{l}) + \nabla \cdot (*\mathbf{r}P) = \mathbf{r} \times \rho\mathbf{g}, \quad (\text{A5})$$

where $\mathbf{l} = \mathbf{r} \times \mathbf{v}$ is the specific angular momentum and $*$ denotes the Hodge star operator. The cross product on the right-hand side vanishes if we assume a monopole potential, and the second divergence term on the left-hand side vanishes when we average over a thin spherical shell

$$\int \nabla \cdot (*\mathbf{r}P) dV = \int_{\partial V} P\mathbf{r} \times d\mathbf{A} = \int_{\partial V} P\mathbf{r} \times \mathbf{n} dA = 0. \quad (\text{A6})$$

Hence we need only take into account the first two terms on the left-hand side when performing a spherical Favre decomposition. Decomposing the velocity and averaging over spherical surfaces yields

$$\frac{\partial\langle\rho\mathbf{l}\rangle}{\partial t} + \nabla_r \cdot \langle\rho(\tilde{u}_r + u_r'')(\tilde{\mathbf{l}} + \mathbf{l}'')\rangle = 0, \quad (\text{A7})$$

where ∇_r denotes the radial part of the divergence operator. Using the usual rules $\langle\rho\tilde{X}\tilde{Y}\rangle = \hat{\rho}\tilde{X}\tilde{Y}$ and $\langle\rho\tilde{X}Y''\rangle = 0$ for correlation terms containing no or only one fluctuating intensive quantity, only two terms remain,

$$\frac{\partial\langle\rho\mathbf{l}\rangle}{\partial t} + \nabla \cdot (\hat{\rho}\tilde{u}_r\tilde{\mathbf{l}}) + \nabla \cdot \langle\rho u_r''\mathbf{l}''\rangle = 0. \quad (\text{A8})$$

This paper has been typeset from a $\text{\TeX}/\text{\LaTeX}$ file prepared by the author.